Symmetry-driven persistent spin texture for the two-dimensional nonsymmorphic CdTe and ZnTe crystal structures

Manish Kumar Mohanta and Puru Jena

Phys. Rev. B **108**, 085432 — Published 29 August 2023

DOI: 10.1103/PhysRevB.108.085432

Symmetry-driven persistent spin texture in two-dimensional nonsymmorphic CdTe and ZnTe crystal structure

Manish Kumar Mohanta* and Puru Jena*

Department of Physics, Virginia Commonwealth University, Richmond, VA 23284, USA

*E-mail: manishkmr484@gmail.com, mohantamk@vcu.edu, pjena@vcu.edu

Abstract: In this work, two non-symmorphic 2D structures of CdTe and ZnTe are modelled, and using state-of-the-art Density Functional Theory and group theory of solids their symmetry-enforced emergent properties are studied. The in-plane ferroelectricity coupled with strong spin-orbit coupling induces a unidirectional out-of-plane Rashba spin-orbit field (SOF) that can host momentum-independent uniform spin configuration known as persistent spin texture (PST) at the Brillouin zone centre. PST in these structures is found to be robust against external perturbations such as strain, structural distortion, and independent of layer thickness. These unprecedented intrinsic spin transport properties hold utmost importance in spintronics as the experimental stringent condition of equal Rashba and Dresselhaus constants [*Phys Rev Lett* **2003**, *90* (14), 146801] is eliminated. The calculated persistent spin helix (PSH) wavelength of less than ~5 nm paves the way for developing next-generation nano-sized non-ballistic spin field-effect-transistors compared to micrometer-size GaAs/AlGaAs quantum wells. Further, these materials exhibit finite spin-Hall conductivity (SHC) at the band edges and, hence, can be used in ferromagnet-free spin-Hall transistors. Although CdTe and ZnTe systems have been widely studied for photocatalysis and solar cell applications over the past few decades, their potential application in spintronic devices has not been explored to date. In particular, mono/few layers of CdTe and ZnTe synthesized from (110) facets of bulk zinc-blende crystals [*Nat. Commun.* **2012**, *3* (1), 1057] satisfy all symmetry operations of the non-symmorphic space group and hence can be considered ideal materials to verify our theoretical results experimentally.

1. Introduction

The post-graphene era has witnessed the prediction, synthesis, and introduction of new quantum materials with emergent functionalities where symmetry, topology, and dimensionality play an important role. [1–4] Electrons possess three degrees of freedom (DoF): charge, spin, and valley. Controlling each DoF for data storage and manipulation leads to three specific research fields; electronics, spintronics, and valleytronics. [5–9] The spin and valley DoFs appear due to relativistic effects and can manifest in materials having strong spin-orbit coupling and requiring certain conditions, such as broken inversion symmetry. [10–12] In recent years, there has been a surge of interest in manipulating spin DoF at the nanoscale. Consequently, extensive theoretical and experimental investigations have been carried out, making the field of spintronics evolve. [13–15]

The spin field effect transistor consists of three components; source, drain, and semiconducting channel material. The source and drain are ferromagnetic materials having a particular spin orientation; the source injects the spin into the semiconducting channel material, and the drain detects the injected spin depending on its relative orientation. [5,7,16] The spin precession can be manipulated by applying an external perpendicular electric field. Recently, there have been experimental interests in redesigning/simplifying conventional spintronic devices; Zhu et al. [15] proposed semiconducting channel materials that show strong spin-orbit coupling, have a large out-of-plane piezoelectric coefficient, and are flexible so that piezo-potential generated by channel material under strain can replace the external electric field. In this regard, Mohanta et al. [17] suggested new hexagonal buckled CdTe and ZnTe monolayers which are direct band gap semiconductors and show significant out-of-plane piezoelectric coefficients. Further, these monolayers exhibit Rashba-type spin splitting at the conduction band minima (CBM) and hence are considered excellent channel material for the next-generation strain-spintronic device. [18,19] Another approach is to eliminate the intrinsic limitation of the spintronic device, such as its short spin lifetime. In a diffusive transport regime, elastic/inelastic electron scattering from the defects and nonmagnetic impurity randomizes the spin due to the momentum-dependent spin-orbit field $\Omega(k)$, which reduces the spin lifetime. The process is known as Dyakonov-Perel spin relaxation [20]. A way to circumvent this process is to make the magnitudes of Rashba and Dresselhaus constants equal [21,22], which can be realized in an experiment by controlling quantum well-width and doping level. [13,14,23–25] Spin-orbit coupled systems generally break the spin rotation symmetry. However, SU(2) rotation symmetry is discovered under these conditions, stabilizing the periodic precession around the unidirectional SOF, known as a persistent spin helix (PSH). [26] An overview of PSH is discussed in Section 2. The PST has been previously observed in bulk systems such as $BiInO_3$ [27], $CsBiNb_2O_7$ [28], and quantum well structures [13,14,23,24]. And recently only a few classes of 2D monolayers have been proposed to support PST. [29–32]

Alternatively, recent theoretical work by Tao et al. [27] demonstrated that the stringent condition of equal Rashba and Dresselhaus constant can be overcome in bulk materials having nonsymmorphic space groups that exhibit intrinsic PST, enforced by symmetry. Nonsymmorphic crystal symmetries [33] combine a fractional lattice translation with either a

mirror reflection (glide plane) or a rotation (screw axis) as schematically presented in Supplemental Materials (SM) Figure S1. [34] The importance of nonsymmorphic crystal symmetry has been widely studied in topological materials where the symmetry-enforced band crossing exists due to nonsymmorphic symmetries alone, independent of the material details. [35–40] In this work, two new non-symmorphic crystal structures are modelled and an in-depth analysis of their symmetry-enforced emergent properties is investigated.

2. Theory of PSH and out-of-plane Spin-Orbit Field (SOF)

2.1 Quantum mechanical perspective

The microscopic origin of the spin-orbit interaction in 2D semiconductors is the absence of inversion symmetry and confining potential. This results in Rashba and Dresselhaus (linear and cubic) spin-orbit terms in the effective Hamiltonian. In the Rashba effect, the spin degeneracy is lifted from spin-orbit coupling under inversion symmetry breaking. Dresselhaus effect is present in semiconductors lacking bulk inversion symmetry such as in zincblende-type structures. [41]

The effective spin-orbit coupling Hamiltonian can be written as

$$H_{SO} = \vec{\Omega}_{SOF}.\vec{\sigma} \quad \ldots\ldots\ldots\ldots\ldots (1)$$

where $\vec{\Omega}_{SOF}$ is the spin-orbit field (SOF) and $\vec{\sigma}$ is Pauli spin matrices. As confirmed experimentally, the cubic term in k only changes the strength of β in equation (2) leaving the Hamiltonian unchanged. [42–44] So, the general form of the Hamiltonian includes linear terms of both Rashba and Dresselhaus contributions for the two-dimensional system and is given by; [21,41,45]

$$\mathcal{H} = \frac{\hbar^2 k^2}{2m} + \alpha\left(k_x\sigma_y - k_y\sigma_x\right) + \beta\left(k_y\sigma_y - k_x\sigma_x\right) \quad \ldots\ldots\ldots\ldots\ldots (2)$$

where $\vec{k}$ is the momentum of the electron confined in a 2D geometry, α, and β correspond to the strengths of Rashba and Dresselhaus spin-orbit coupling, respectively, and m is the effective electron mass. The Rashba coefficient α is tunable using an external electric field perpendicular to the plane of the 2D electron gas whereas the Dresselhaus constant β depends on the semiconductor material and the geometry of the sample.

The energy dispersion of this Hamiltonian leads to two branches.

$$\varepsilon_{\pm}\left(\vec{k}\right) = \frac{\hbar^2 k^2}{2m} \pm \sqrt{(\alpha k_y + \beta k_x)^2 + (\alpha k_x + \beta k_y)^2} \quad \ldots\ldots\ldots\ldots\ldots (3)$$

For zero value of coupling constants α or β, the dispersions are isotropic and Fermi contours are concentric circles whereas, for non-zero α and β, the energy contour plots are anisotropic having (1,1) and (1, -1) directions as symmetry axes. [46] The spin rotation symmetry is generally broken in spin-orbit coupled systems. However, particularly for $\alpha = \pm\beta$, a new type of special unitary SU(2) spin rotation symmetry $\Sigma = (\sigma_x \pm \sigma_y)/\sqrt{2}$ is discovered that leaves the Hamiltonian invariant, $[\mathcal{H}, \Sigma] = 0$. [22,26] Under this condition, the electron's spin-up and spin-down states become independent of the wave vector and, hence, prevent the

randomization of the spin. The electron spin undergoes a controlled rotation known as the persistent spin helix (PSH). Additionally, previous investigation indicates that under certain relations between the Rashba constant and radius of curvature in a rolled-up 2D electron gas, tangential spin can be preserved. [47]

The Hamiltonian can be formulated for $\alpha = \pm\beta$ as [22];

$$\mathcal{H} = \frac{\hbar^2}{2m}[k^2 + 2(\vec{k}.\vec{Q})\Sigma] \text{ ..... (4)}$$

The energy dispersions form circles whose centres are displaced from the Γ point by shifting wave vector $\vec{Q}$.

$$\varepsilon_{\pm}(\vec{k}) = \frac{\hbar^2}{2m}[k^2 \pm 2(\vec{k}.\vec{Q})] \text{ ..... (5)}$$

The spin-up and spin-down bands have an important shifting property [26]:

$$\varepsilon_{\downarrow}(\vec{k}) = \varepsilon_{\uparrow}(\vec{k} + \vec{Q}) \text{ ..... (6)}$$

Recent theoretical [27] work suggests that PST can be imposed by symmetry, overcoming the condition of equal Rashba and Dresselhaus parameters. In this regard, a new class of quantum materials having orthorhombic nonsymmorphic crystal structures such as SnTe, GeTe thin films, Bi (110) exhibiting strong SOC and extra symmetries like glide plane reflection symmetries have been proposed to realize an out-of-plane Rashba effect $\Omega^z_{SOF}(\vec{k})$. [32,48,49] In these materials, the in-plane electric field in a 2D electron system can generate a unidirectional SOF expressed by;

$$\vec{\Omega}_{SOF}(\vec{k}) = \alpha(\hat{E} \times \vec{k}) \text{ ..... (7)}$$

Application of the in-plane electric field $\vec{E}$ ($\hat{E}$ represents field direction) parallel to $\hat{x}$ yields a SOF with the following term:

$$\vec{\Omega}_{SOF}(\vec{k}) = \alpha(\hat{x} \times \vec{k}) = \alpha k_y \hat{z} \text{ ..... (8)}$$

This unidirectional perpendicular SOF, referred to as the out-of-plane Rashba effect, is induced by the in-plane electric field and has an identical form in the III-V quantum well grown along [110] direction. [21] The Hamiltonian can be written as;

$$\mathcal{H} = \mathcal{H}_{kin} + \vec{\Omega}_{SOF}.\vec{\sigma} = \frac{\hbar^2}{2m}(k_x^2 + k_y^2) + \alpha k_y \sigma_z \text{ ..... (9)}$$

For a ferroelectric material, built-in polarization generates the in-plane electric field and, hence, the SOF induced by the ferroelectric polarization (*P*) can be written as;

$$\vec{\Omega}_{SOF}(\vec{k}) = \alpha(\hat{P} \times \vec{k}) \text{ ..... (10)}$$

where $\hat{P}$ is the direction of ferroelectric polarization that replaces $\hat{E}$ in equation (7).

2.2 Group theory perspective

Recent work by Tao et al. [27] has demonstrated that PSH can be an intrinsic property of a material if it belongs to a non-symmorphic space group crystal structure. In general, the symmetry operations of the non-symmorphic space group No. 31 are given by;

$$\left\{\langle Ee|\{0,0,0\}\rangle, \langle C_{2z}|\ \left\{\frac{1}{2},0,\frac{1}{2}\right\}\rangle, \langle IC_{2y}|\ \left\{\frac{1}{2},0,\frac{1}{2}\right\}\rangle, \langle IC_{2x}|\ \{0,0,0\}\rangle\ \right\} \ldots\ldots\ldots\ldots (11)$$

The two-fold rotations followed by inversion symmetry (IC_{2y}) leads to mirror reflection symmetry ($\widehat{M}_{zx}$) and hence the terms in equation (11) can be written as

$$\{E, \hat{C}_{2z}, \widehat{M}_{zx}, \widehat{M}_{yz}\} \ldots\ldots\ldots (12)$$

Here, the translational terms are excluded. A more detailed explanation of symmetry operations is provided in Table S1 in SM.

Since PSH is shown to originate from SU(2) rotational symmetry in earlier work [26] and also from crystal symmetry [27], a one-to-one correlation between rotational symmetry operation in SU(2) and crystallographic point group must exist. SU(2) is a group of unitary matrices and has three generators;$\{ i\sigma_x, i\sigma_y, i\sigma_z\}$ (see section S.1 and S.2 in SM for more details).

The crystal structure of the 2D non-symmorphic space group is invariant under several point group operations $\{E, \hat{C}_{2x}, \widehat{M}_{zx}, \widehat{M}_{xy}\}$ similar to equation (12) listed in Table 1. [31] Considering transformation rules in Table 1 and C_{2v} point group symmetry operation, it can be shown that the unidirectional SOF is protected by M_{xy} as Ω^z_{SOF} survives under the in-plane mirror reflection whereas Ω^z_{SOF} becomes an odd function under the vertical mirror reflection M_{zx}; $\Omega^z_{SOF}(k_x, -k_y) = -\Omega^z_{SOF}(k_x, k_y)$. [32]

Table 1 Transformation rules for wave vector (k), Pauli matrices (σ) under time-reversal symmetry, implying a reversal of both spin and momentum ($\hat{T}$) and C_{2v} point group symmetry operation $\widehat{C}_{2x}$, $\widehat{M}_{xy}$, $\widehat{M}_{zx}$ for the Γ-point in the first Brillouin zone.

Symmetry operation	(k_x, k_y)	$(\sigma_x, \sigma_y, \sigma_z)$
$\hat{T} = i\sigma_y K$; K is complex conjugation	$(-k_x, -k_y)$	$(-\sigma_x, -\sigma_y, -\sigma_z)$
$\hat{C}_{2x}$	$(k_x, -k_y)$	$(\sigma_x, -\sigma_y, -\sigma_z)$
$\widehat{M}_{xy}$	(k_x, k_y)	$(-\sigma_x, -\sigma_y, \sigma_z)$
$\widehat{M}_{zx}$	$(k_x, -k_y)$	$(-\sigma_x, \sigma_y, -\sigma_z)$

3. Results and discussion

3.1 Atomistic modelling of an ideal non-symmorphic 2D crystal structures, symmetry analysis, and stability

Using the group theory of solids supported by DFT results, Tao and Tsymbal [27] have demonstrated that intrinsic PST can be enforced by non-symmorphic space group symmetry in

certain bulk materials. Following previous reports, two-atomic thick non-symmorphic crystal structures composed of Cd-Te and Zn-Te have been modelled using the same bond length and bond angles between the atoms as that of respective bulk zincblende crystal structures. [50] The same approach has been adopted in earlier work [27] for analyzing the symmetry-enforced properties excluding any additional effects from structural perturbation. Particularly, CdTe and ZnTe are considered for modelling in this study as Mohanta et al. [17] have recently reported Rashba spin splitting in CdTe and ZnTe hexagonal buckled structures. The ideal non-symmorphic structures are modelled to generalize the properties originating from crystal symmetry and thus thickness dependance is excluded. Detailed geometrical parameters of our designed structures are listed in Table 2. Each unit cell contains four atoms having four symmetry operators that leave the atomic configurations invariant; (i) identity operation *E*; (ii) twofold screw rotation $\overline{C}_{2x}$ (twofold rotation around the *x*-axis, $\hat{C}_{2x}$, followed by a translation of $\tau = \frac{a}{2}, \frac{b}{2}$) where *a* and *b* are the lattice parameters along the x and *y* axis respectively; (iii) glide reflection (G or $\overline{M}_{xy}$) (reflection with respect to the *xy* plane followed by translation τ); and (iv) reflection M_{zx} with respect to the *zx* plane. The top and side views of the non-symmorphic CdTe and ZnTe crystal structures along with mirror (M_{zx}) and glide reflection (*G*) symmetries are indicated in Figure 1. The designed crystal structures exhibit nonsymmorphic symmetry through a glide-mirror operation; reflection about z=0 plane (M_{xy}) followed by a translation of $a/2$ and $b/2$ along the *x* and *y* axis, respectively. As illustrated in Figure 1(c), starting from the Cd at atomic site 'A', mirror reflection (M_{xy}) brings it to site 'B' which is not allowed in the structure. An additional fractional translation t: $(a/2, b/2, 0)$ is needed to bring it to the allowed atomic site 'C'. As can be seen from the top view in Figure 1, the relative positions of the constituent atoms with respect to the crystal axis are opposite in CdTe and ZnTe unit cells and hence the ferroelectric polarization direction will be opposite to each other which will be discussed later. The nonsymmorphic groups are more numerous than the symmorphic groups and these crystals extensively occur in nature. For example, the diamond crystal structure belongs to the nonsymmorphic space group. Recently several monolayers having non-symmorphic crystal symmetry have been proposed and synthesized; phosphorene [51], SnS, SnSe, GeS, GeSe [52], SnTe monolayer [53], GeTe [54], Bi (110) monolayer [48,55], group-VA [56].

To check the dynamical stability of the unit cells, phonon dispersions of both structures are plotted in Figure 1(d). The vibration of four atoms in the unit cell leads to twelve phonon modes out of which three are acoustic and nine are optical phonon branches. The positive phonon frequency of both acoustic and optical modes indicates that the bonds between the atoms have sufficient restoring force to retain their original symmetry, bond length, and bond angles, thus confirming their structural stability. Since the designed structures are stable, a systematic investigation of electronic properties has been conducted to shed light on (i) intrinsic persistent spin helix (PSH) in these 2D structures enforced by symmetry, (ii) the effect of ferroelectric switching/polarization ($\pm P$) on spin polarization and (iii) the effect of external perturbations such as vertical electric field and biaxial strain on PST, (iv) feasibility of experimental realization and application in spin-Hall effect transistor.

Table 2 Geometrical parameters of modelled nonsymmorphic structures: lattice constants a, b; bond length (a_1, a_2) and bond angle (θ_1, θ_2), the vertical distance between atomic layers (d)					
Systems	a (Å)	b (Å)	a_1=a_2 (Å)	$\theta_1 = \theta_2$ (degree)	d (Å)
Orthorhombic CdTe (o-CdTe)	6.56	4.64	2.84	109.47	2.32
Orthorhombic ZnTe (o-ZnTe)	6.11	4.32	2.64	109.47	2.16

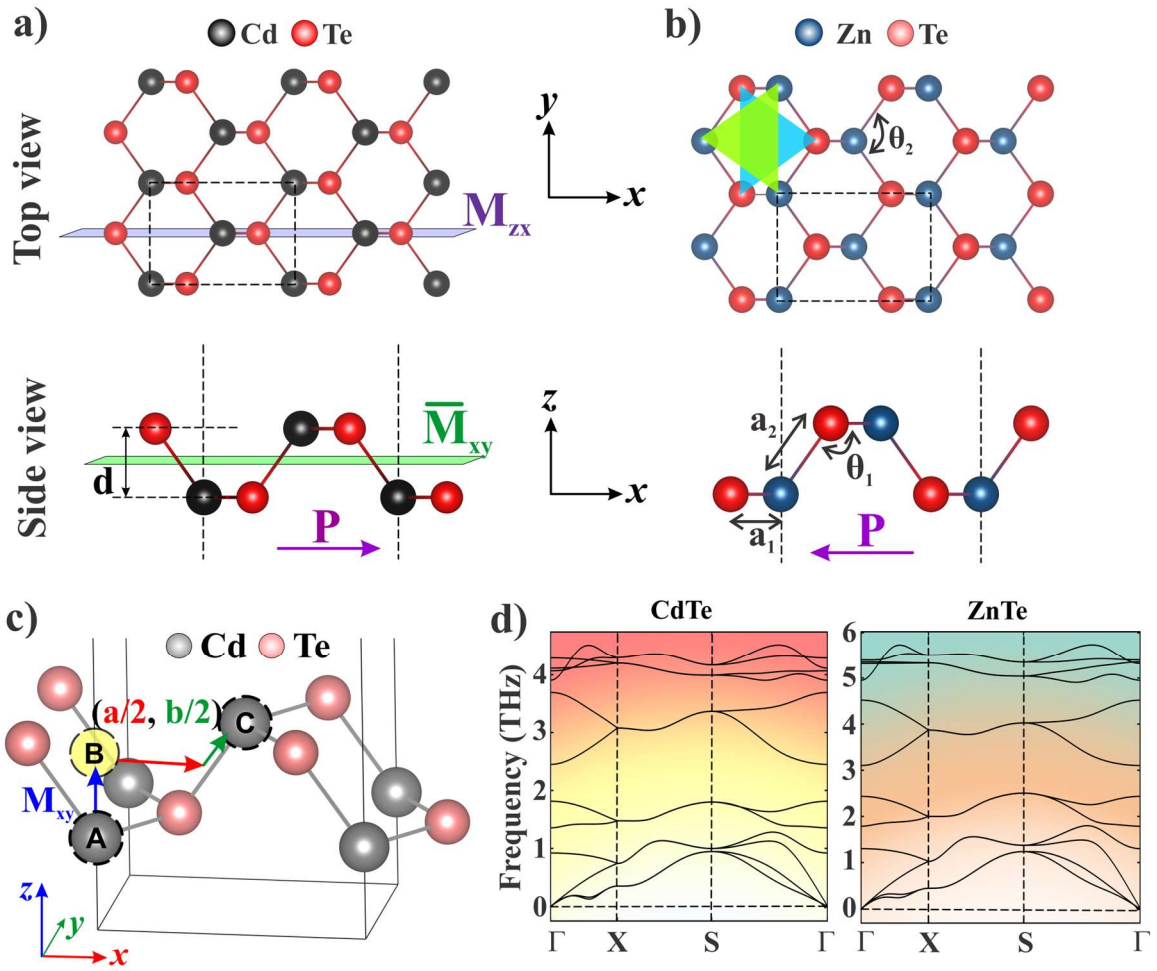

Figure 1 (a, b) Top and side view of designed 2D non-symmorphic CdTe and ZnTe crystal structures; the unit cell is marked by a dashed line, mirror symmetry M_{zx}, glide plane symmetry G or $\overline{M}_{xy}$, and direction of ferroelectric polarization in the unit cell is indicated, (c) illustration of a nonsymmorphic group operation on CdTe modelled structure includes mirror reflection A→B and a translation B→C, (d) phonon dispersion plot of CdTe and ZnTe along the high symmetry direction of rectangular Brillouin zone; Γ (0,0,0)→X (0.5,0,0)→S (0.5,0.5,0) → Γ(0,0,0).

3.2 Ferroelectric polarization and spatial inversion operator

The ferroelectricity is originated from non-centrosymmetric symmetry as indicated by coloured triangles in Figure 1(b) and non-symmorphic element in the crystal structure which breaks the local structural mirror symmetry and forms dipole moment. The direction of ferroelectric polarization ($\vec{P}$) is opposite to each other in CdTe (+x) and ZnTe (-x). For a 2D system, under spatial inversion operator or C_{2z} operator (180-degree rotation around the z-axis), the wave vector transformed as $(k_x, k_y) \xrightarrow{I} (-k_x, -k_y)$ and so as the ferroelectric polarization; $\vec{P} \xrightarrow{I} -\vec{P}$. [29,57] The magnitudes of the in-plane ferroelectric polarization in the unit cell are calculated to be 2.22×10^{-1} C/m and 2.32×10^{-10} C/m for CdTe and ZnTe, respectively, which are comparable to other ferroelectric 2D materials; functionalized MXenes ($4.93 - 6.25 \times 10^{-10}$ C/m) [58], In_2Se_3 (2.59×10^{-10} C/m) [59], GeS (5×10^{-10} C/m) [60], Bi(110) monolayer (0.47×10^{-10} C/m) [48].

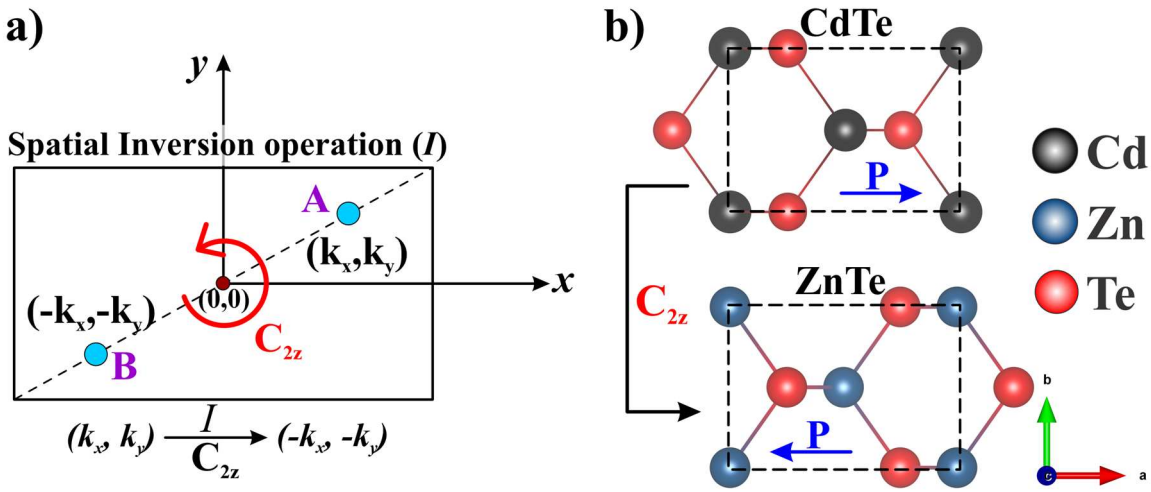

Figure 2 (a) Schematic representation of spatial inversion operation in 2D system $I(k_x, k_y) \rightarrow (-k_x, -k_y)$; point B is the final position of point A under spatial inversion operation (***I***) which can be obtained by C_{2z} symmetry operation in the crystal structure, (b) illustration of spatial inversion symmetry and direction of ferroelectric polarization ($\vec{P}$); $\vec{P} \xrightarrow{I/C_{2z}} -\vec{P}$.

3.3 Electronic properties with and without spin-orbit coupling

The electronic band structure of nonsymmorphic CdTe and ZnTe are plotted in Figure 3. From the electronic band dispersion, these materials are found to be direct band gap semiconductors with band edges; conduction band minima (CBM), and valence band maxima (VBM) located at the Brillouin zone centre. The atom-projected band structure indicates that VBM is mainly contributed by Te-atoms whereas CBM is contributed by both Cd and Te-atoms, which can be confirmed from the band-decomposed charge density plot in Figure 3. The band gaps obtained using different functionals are listed in Table 3. These values indicate that the band gap lies in the visible region and is comparable to the values in well-known MoS_2 (~1.8 eV) [4,61] and WS_2 (~2.1 eV) [62]. Hence, these materials can have the potential for

electronics and optoelectronics applications. Previously CdTe and ZnTe monolayers/thin films of different geometry had been extensively studied for solar cell and catalysis applications. [63–69]

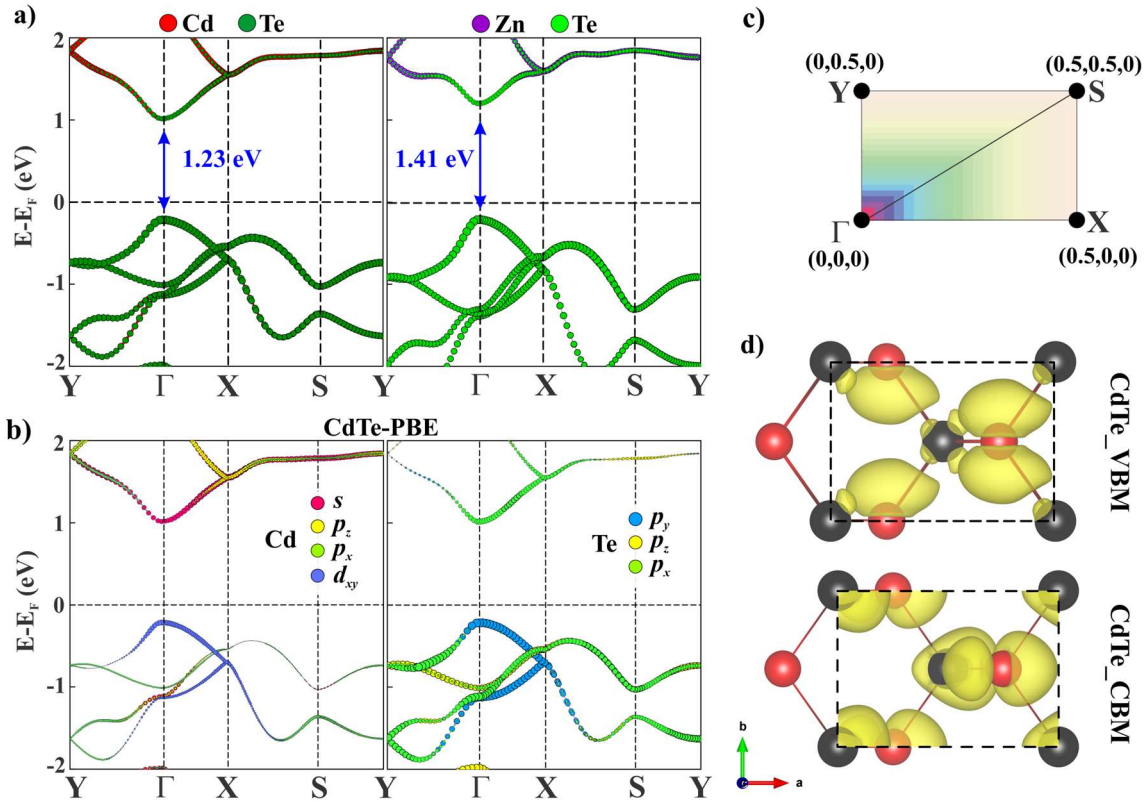

Figure 3 (a) Calculated atom-projected electronic band dispersion of CdTe and ZnTe 2D structures using GGA-PBE, (b) orbital projected band structure of CdTe, (c) schematic of Brillouin zone of a rectangular unit cell, (d) band decomposed charge density of CdTe correspond to band edges with an iso-surface value of 0.0025 e/Å^3.

Further, since both these structures contain heavy tellurium atoms, the relativistic effect is incorporated in electronic properties calculation, and the spin-projected band structure is plotted in Figure 4. The effect of SOC can be observed in the band dispersion plot as the band gap decreases (refer to Table 3). There are two very interesting notable observations in the band structure; (i) Rashba-type spin splitting occurring at both CBM and VBM, (ii) the spin splitting occurs along $\Gamma \rightarrow Y$ direction, whereas the spin states remain degenerate along the $\Gamma \rightarrow X$ line. The first observation can be explained by the orbital contributions of band edges and the direction of ferroelectric polarization in the system. From the orbital projected band structure in Figure 3, the band edges are confirmed to be contributed by in-plane Cd_d_{xy} and Te_p_x atomic orbitals and the ferroelectric polarization is along the $+x$-axis (P_x/E_x). Hence, the Rashba-type spin splitting is observed in both CBM and VBM; $\langle d_{xy}|E_x|d_{xy}\rangle \neq 0$ and $\langle p_x|E_x|p_x\rangle \neq 0$. [17,19,70]

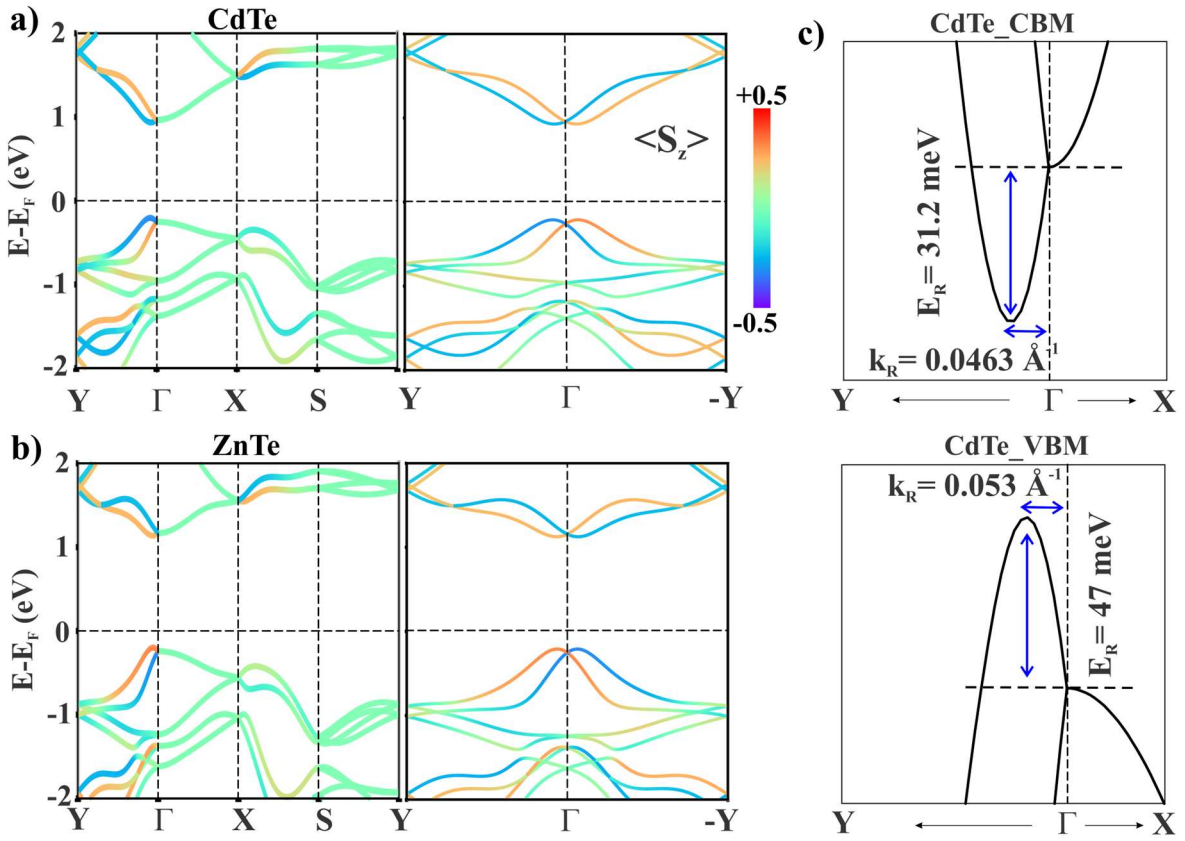

Figure 4 (a, b) Spin-projected electronic band structure of CdTe and ZnTe including relativistic effect, (c) zoomed image of CBM and VBM of CdTe at Γ-point.

Now the origin of the degenerate state along $\Gamma \rightarrow X$ line in the presence of SOC can be explained using the symmetry of the wave vector $\vec{k}$ which is invariant under $\overline{C}_{2x}$ screw rotation and $\overline{M}_{xy}$ glide mirror reflection symmetry. Since the Pauli matrices are anti-commutative $\{\sigma_x,\sigma_z\}=0$ in nature, hence the operators (refer to equation s4 in SM) follow the same; $\{\overline{C}_{2x},\overline{M}_{xy}\}=\{i\sigma_x, i\sigma_z\}=0$ on the line $\Gamma \rightarrow X$. Now, for an eigenvector $|\psi_m\rangle$ of $\overline{M}_{xy}$ operator with the eigenvalue of m the following can be obtained;

$$\overline{M}_{xy}|\psi_m\rangle = m|\psi_m\rangle \ldots\ldots\ldots\ldots (13)$$

$$\overline{M}_{xy}\overline{C}_{2x}(|\psi_m\rangle) = -\overline{C}_{2x}\overline{M}_{xy}|\psi_m\rangle = -m\overline{C}_{2x}|\psi_m\rangle = -m\,(\overline{C}_{2x}|\psi_m\rangle) \ldots. (14)$$

Equations (13) and (14) indicate that $|\psi_m\rangle$ and $\overline{C}_{2x}|\psi_m\rangle$ are different states with the same eigenvalue m, thus ensuring the double degeneracy along the $\Gamma \rightarrow X$ line.

Also, the same result can be obtained using equation (10), the Rashba SOF $\vec{\Omega}_{SOF}(\vec{k}) = \alpha(\pm\hat{P}_x \times \vec{k}_x) = 0$ along the $\Gamma \rightarrow X$ line. Here, $\pm\hat{P}_x$ corresponds to polarization direction in CdTe and ZnTe structures, respectively.

The energy eigenvalues of the effective Hamiltonian of the 2D system presented in Equation 9 i.e., $H = E_0(k) + \alpha k_y \sigma_z$ are given by; [71]

$$E^{\pm}(k) = E_0(k) \pm \alpha k_y \text{ ..... (15)}$$

Equation (15) represents the spin splitting along $\Gamma \rightarrow Y$ directions and also leads to the following shifting property $\varepsilon_{\downarrow}(\vec{k}) = \varepsilon_{\uparrow}(\vec{k} + \vec{Q})$ where $\vec{Q}$ is the shifting wave vector given by;

$$\vec{Q} = \frac{2m_y^*\alpha}{\hbar^2}[0,1,0] \text{ ..... (16)}$$

Here, m_y^* is the effective mass of an electron along $\Gamma \rightarrow Y$ direction and α is the Rashba constant. The shifting wave vector can be depicted in Figure 5. The strength of spin-orbit coupling known as the Rashba parameter (α) along $\Gamma \rightarrow Y$ direction can be calculated from the band dispersion using equation (17). The results are listed in Table 3.

$$\alpha = \frac{2E_R}{k_R} \text{ ..... (17)}$$

Here, E_R is the energy difference between the energies at the peak and the high symmetry point, k_R is the momentum offset between the peak and the high symmetry point as marked in Figure 4(c). The calculated value of the Rashba constant is nearly the same for both CdTe and ZnTe. For comparison, a list of Rashba constant values of other 2D Rashba materials is provided in Table 3.

Table 3 Calculated band gap of o-CdTe and o-ZnTe using different functionals.

System	E_g^{PBE} (eV)	$E_g^{PBE+SOC}$ (eV)	E_g^{HSE} (eV)	Γ→Y	
				α_R^{CBM} (eVÅ)	α_R^{VBM} (eVÅ)
o-CdTe	1.23	1.14	1.81	1.35	1.77
o-ZnTe	1.41	1.33	2.1	1.37	1.79
Reported Rashba constant values of other 2D materials for comparison					
2D materials				CBM	VBM
Buckled CdTe [17]				1.27	/
Buckled ZnTe [17]				1.06	/
BiSb [72]				2.3	/
WA_2Z_4 [73]				/	0.87-1.8
AlBi [70]				2.77	/
WSeTe [74]				/	0.92
$PtSe_2/MoSe_2$ [75] heterostructure				/	1.3
BiTeX [76]				1.86	/

Now to visualize the spin polarization direction in the designed structures, the spin texture is plotted at a constant energy above and below the Fermi level in Figure 5 which indicates its unidirectional (S_z) nature. Note that the ferroelectric polarization directions are opposite in CdTe and ZnTe as discussed in section 3.2. Comparison of the spin texture plots provides a qualitative understanding of the relationship between spin polarization direction and ferroelectric polarization. This can be explained in two ways. [29,57]

(i) Let the Bloch wave functions of two states with opposite ferroelectric polarization be represented by $|+P,k\rangle$ and $|-P,k'\rangle$ where P and k are ferroelectric polarization and wave vector, respectively. Considering the wave function $|+P,k\rangle$, the transformation under spatial inversion symmetry (I) is given by; $I|+P,k\rangle = |-P,-k\rangle$ where both ferroelectric polarization and wave vector reversed their direction. Under time-reversal symmetry ($\hat{T}$), the wavefunction transformed to $\hat{T}|+P,k\rangle = |+P,-k\rangle$, where the direction of ferroelectric polarization remains intact. Here, time-reversal symmetry is included since the spin reverses its direction (spin-up and spin-down) under the time reversal operator. Some properties of the time reversal symmetry operator $\hat{T}$ is listed in Table S2 in SM. Now, under both time reversal and inversion symmetry, the given wave function is transformed to $\hat{T}I|+P,k\rangle = |-P,k\rangle$. Considering these transformation rules, the behavior of spin polarization direction with ferroelectric polarisation can be explained. The expectation value of the spin operator $\langle S\rangle$ can be obtained as follows; [29,57]

$$\langle S\rangle[-P,k] = \langle -P,k|S|-P,k\rangle = \langle +P,k|I^{-1}T^{-1}STI|+P,k\rangle = \langle +P,k|-S|+P,k\rangle = \langle -S\rangle[+P,k] \quad \ldots\ldots\ldots\ldots\ldots (18)$$

Equation (18) clearly describes reversible spin polarization direction by ferroelectric switching using symmetry analysis.

(ii) Also, the orientation of spin texture with the direction of polarization can be directly obtained from equation (10).

$$\text{For } +\hat{P}\text{: } \vec{\Omega}_{SOF}(\vec{k}) = \alpha\left(+\hat{P}\times\vec{k}\right) = \alpha k_y(+\hat{z}) \quad \ldots\ldots\ldots (19)$$

$$\text{For } -\hat{P}\text{: } \vec{\Omega}_{SOF}(\vec{k}) = \alpha\left(-\hat{P}\times\vec{k}\right) = \alpha k_y(-\hat{z}) \quad \ldots\ldots\ldots (20)$$

Equation (19-20) indicates the reversible nature of spin orientation with ferroelectric polarization as demonstrated in Figure 4-5. Note that recent experimental work demonstrated purely in-plane ferroelectricity at room temperature in monolayer SnS [77] which has a similar crystal structure.

The spatially periodic mode of PSH also known as the pitch/wavelength of PSH can be calculated using the following relation;

$$l_{PSH} \equiv \frac{2\pi}{|\vec{Q}|} = \frac{\pi\hbar^2}{m_y^*\alpha} \quad \ldots\ldots\ldots\ldots (21)$$

For practical application of the out-of-plane Rashba effect, the coherent spin precession of the PSH can be used to fabricate a spin transistor with a size that is determined by l_{PSH}. [22,32,78] The short pitch size of a rapidly precessing PSH is highly desirable. All the variables for the calculation of l_{PSH} are listed in Table 4 and are found to be ~ 4 nm and 5 nm for o-CdTe and o-ZnTe respectively. To design ultrathin spin-FET having a channel length of l_{PSH}, a material having a large Rashba coefficient (α) is required. Therefore, the 2D ferroelectric materials consisting of heavy elements that possess large atomic spin-orbit coupling are of interest.

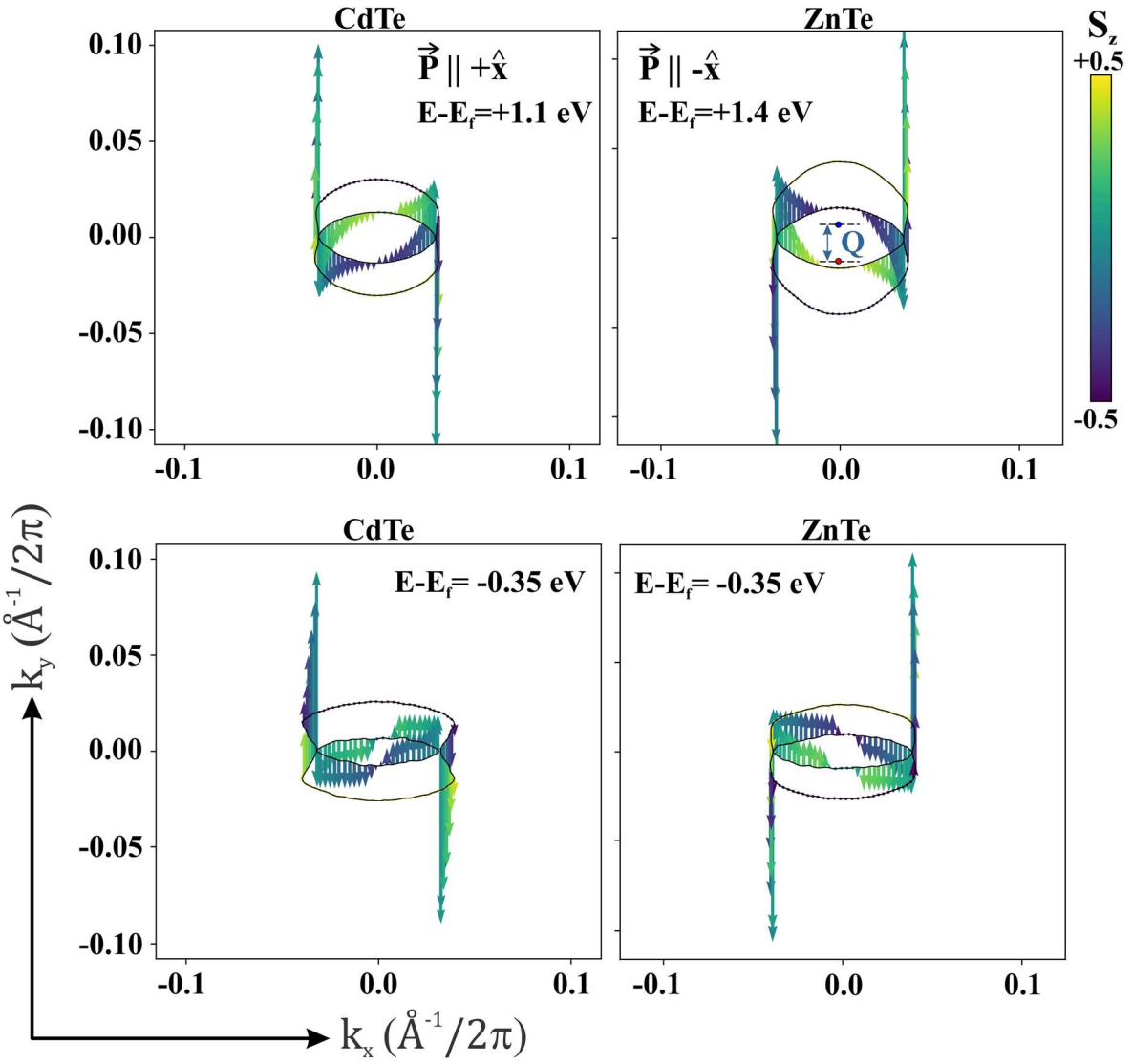

Figure 5 Spin-projected constant energy contour plots of spin texture calculated in k_x-k_y plane centered at Γ-point; reference fermi energy is zero. The arrow represents spin polarization direction $\pm z$.

Table 4 Calculated effective mass of the electron, Rashba constant, and the pitch of PSH (l_{PSH}) of the conduction band			
Systems	Effective mass of the electron m^*/m_0 along $\Gamma \rightarrow Y$	Rashba constant (α) (eV.Å)	l_{PSH}
o-CdTe (thickness 2.32 Å)	0.392	1.35	4.5 nm
o-ZnTe	0.442	1.37	3.9 nm
$BiInO_3$ bulk [27]	0.61	1.91	2 nm

SnTe (001) thin film [32]	/	/	8.8-18.3 nm
GaAs/AlGaAs (001) quantum wire [23]	/	/	7-10 μm

3.4 Effect of vertical electric field on PSH and spin-Hall transistor

Next, the effect of external perturbations such as perpendicular electric field (E-field) and biaxial strains on electronic properties are studied. A vertical E-field is applied perpendicular to the plane of the 2D structures. The resulting band gap variation is plotted in Figure 6(a). Although there is a slight decrease in the band gap with increasing electric field, beyond the critical field of 0.3 V/Å for both CdTe and ZnTe, near free electron gas (NFEG) states appear in the band structure that closes the band gap. These states are surface-induced unoccupied empty states, parabolic, and move towards the Fermi level with increasing electric field at the Γ-point as seen in other 2D systems. [79,80] For a non-zero vertical electric field, the out-of-plane spin polarization is significantly affected which leads to spin decoherence and can be depicted in Figure 6(c). The complications in the spin texture plot arise because of the addition of a new perturbation term in the Hamiltonian which leads to different energy.

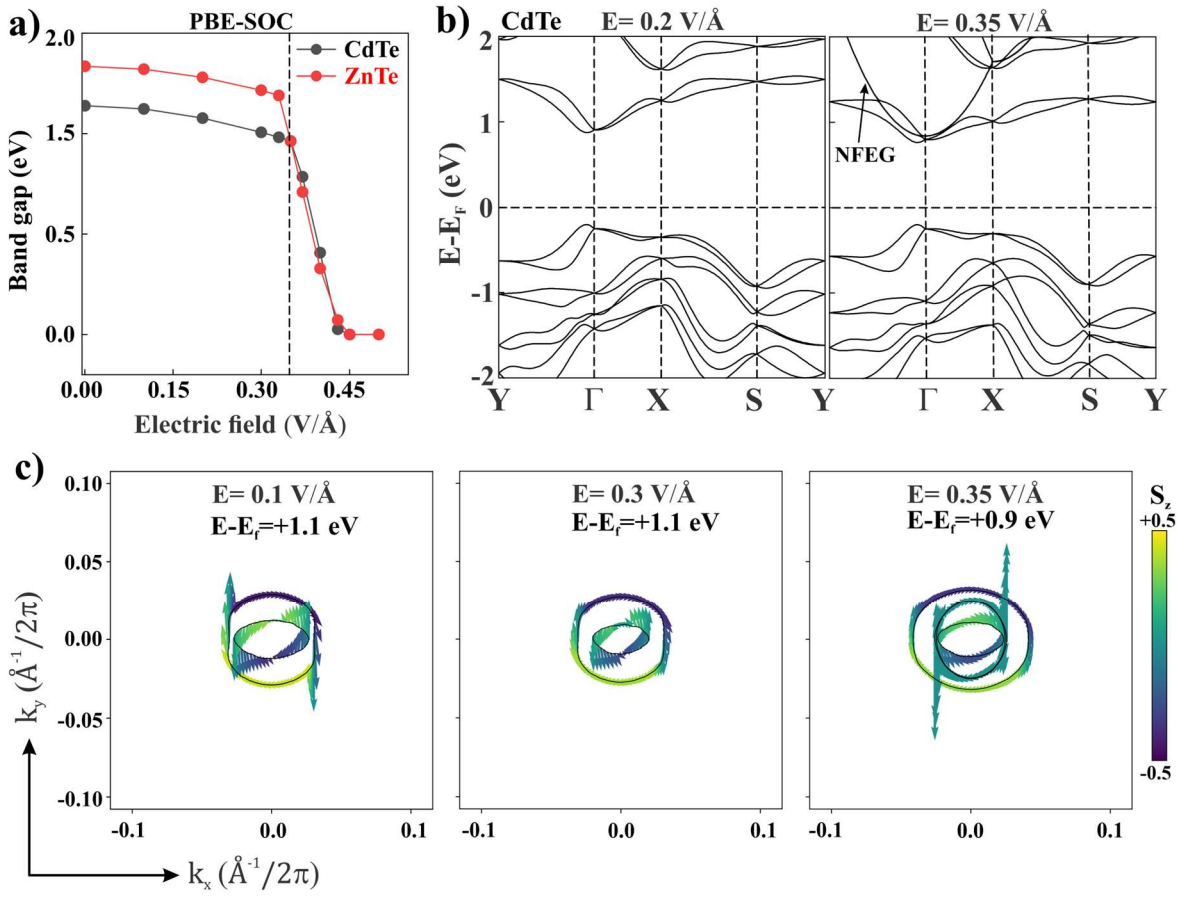

Figure 6 (a) Calculated band gap variation under perpendicular electric field, (b) band dispersion and (c) evolution of spin-texture plot of CdTe under different electric field strength.

Further, the spin-Hall conductivity (SHC) is calculated for both 2L-CdTe and ZnTe structures and plotted in Figure 7(a). A finite SHC can be observed at the band edges. Motivated by the previous reports [49,81] and based on our results, a spin-Hall transistor [82–84] (SHT) is proposed as illustrated in Figure 7(b). The SHT device has three regions R-I, R-II, and R-III which represent spin injection, gate-controlled, and spin collector regions, respectively. The spin from R-I can be injected into R-II via the spin Hall effect (SHE) where the charge current along the y-direction is converted into a transverse spin current polarized along the z-axis. In R-II, the out-of-plane SOF induces PSH mode in the crystal, which can be modulated using a vertical electric field (E_z) applied using the gate electrode. For E_z=0, the PSH mode is maintained and hence the polarized spins do not lose the spin information and collected in R-III. Using the inverse spin Hall effect (ISHE), the spin current is converted back into charge current along the y-direction which generates the Hall voltage as schematically presented in Figure 7(b). For non-zero E_z in R-II, the spin decoherence occurs which reduces the spin lifetime. Hence, the Hall voltage decreases. In other words, the PSH mode can be broken via non-zero vertical electric field.

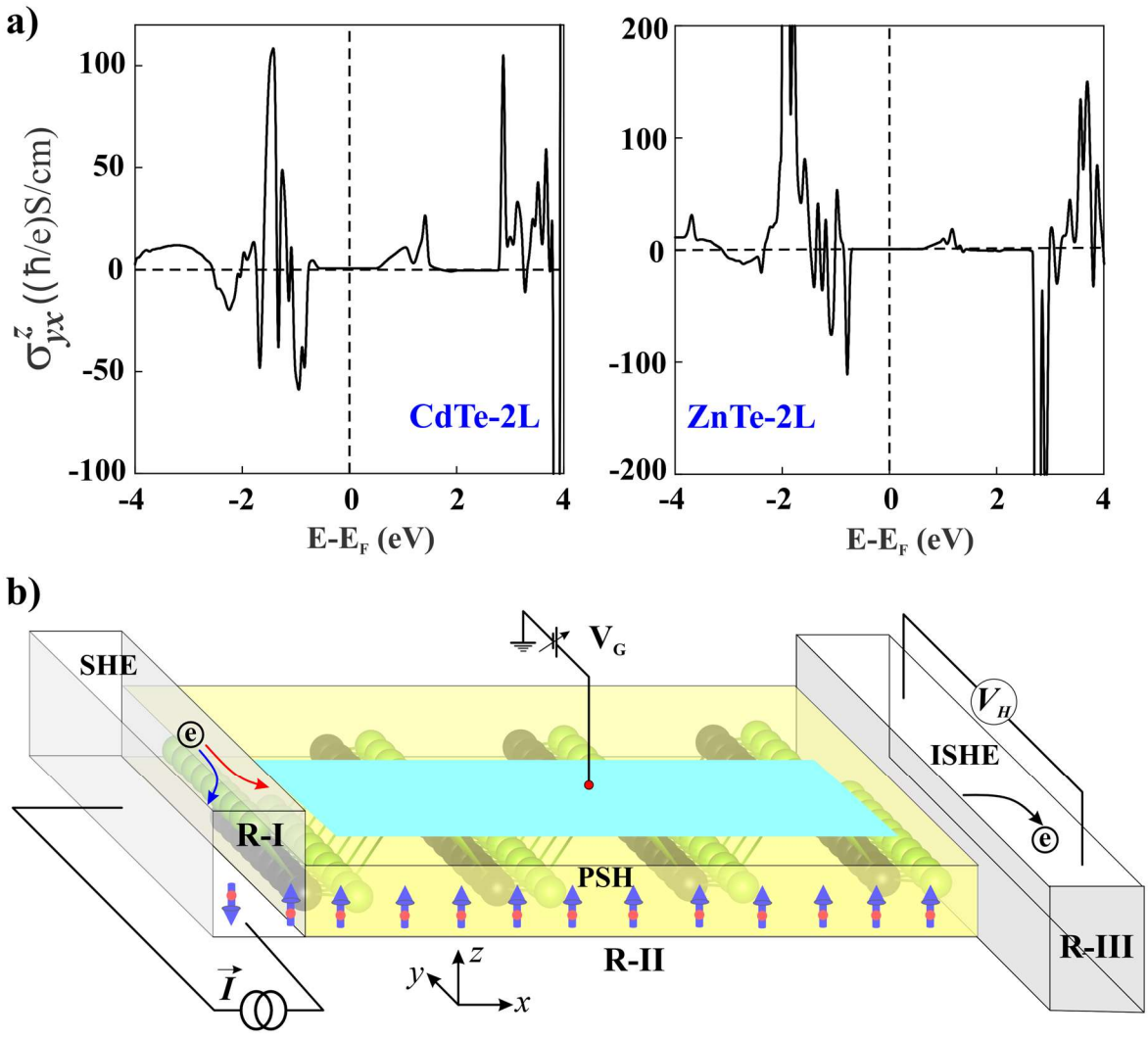

Figure 7 (a) Calculated spin-Hall conductivity for 2L-CdTe and ZnTe, (b) schematic of a spin-Hall effect transistor.

3.5 Effect of biaxial strain on PST

Strain engineering can be an effective tool to manipulate the electronic properties such as the transformation of semiconducting to metallic or direct band gap to indirect band gap [85–88] and it is possible using different experimental techniques such as AFM tips, bending on a flexible substrate, or interfacial lattice mismatch. [89–92] In this regard, a small biaxial strain of up to $\pm$5% is applied and electronic properties under strain are studied. Strain is defined as $\epsilon = \frac{a-a_0}{a_0}$; where a_0 and a are the unstrained and strained lattice constants, respectively. From the electronic dispersion plotted in Figure 8(a), significant change in the band gap as well as the spin splitting is observed. The band gap of increases and decreases under compressive and tensile strain respectively. The linear variation of the Rashba constant calculated from the band dispersion under biaxial strain is observed in Figure 8(b). Hence, the magnitude of out-of-plane SOF which depends on the Rashba constant as in equation (8); $\vec{\Omega}_{SOF}(\vec{k}) = \alpha k_y \hat{z}$ can be manipulated. Nevertheless, the PST is found to be robust against biaxial strain.

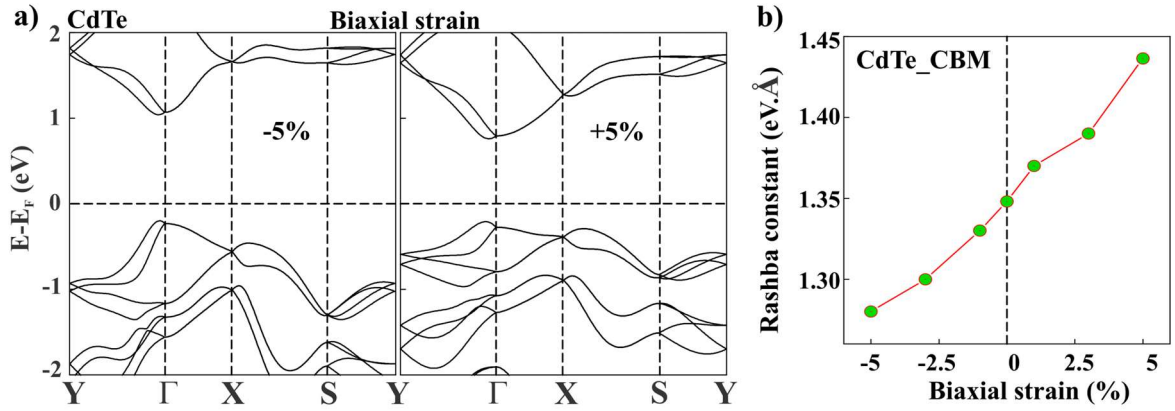

Figure 8 (a) Calculated band dispersion of CdTe under biaxial strain, (b) variation of the Rashba constant under biaxial strain.

Next, the dependency of spin-transport properties on layer thickness and crystal structures having different symmetry are studied and can be depicted in Figure 9. With increasing the layer thickness the band gap decreases significantly but the PST state enforced by unidirectional SOF is maintained in the system and the same can be seen in the spin-projected band structure plot in Figure 9(b). The other crystal structures such as hexagonal systems do not exhibit PST. Although hexagonal planar CdTe monolayers do not show any spin-dependent properties, buckled structures exhibit Rashba splitting at CBM due to the built-in out-of-plane electric field E_z in the system coupled with p_z orbitals i.e.; $\langle p_z|E_z|p_z\rangle \neq 0$. [17,19,70] A finite out-of-plane spin-polarized splitting occurs at the high symmetry K-point in a hexagonal buckled crystal structure. Such type of spin splitting is called valley spin splitting which has been identified in a previous work [19] in a similar system. The working principle of valleytronics is very different from spintronics and can be found elsewhere. [10,93]

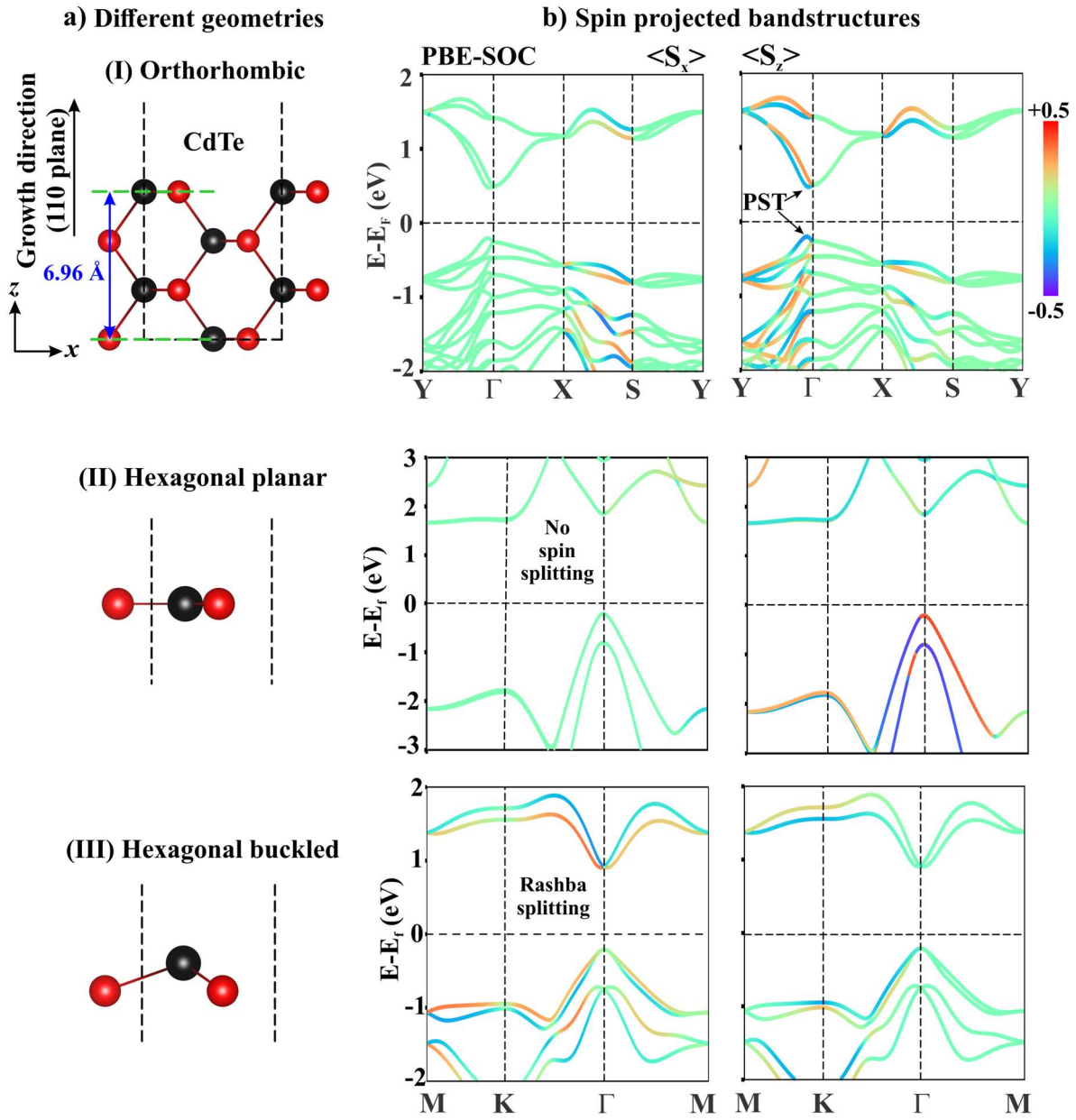

Figure 9 Comparative plot of (a) different atomic arrangement of CdTe in the unit cell and (b) corresponding spin projected S_x and S_z band structure.

3.5 Effect of deformed crystal structure on PSH and experimental realization

In the previous sections, 2D nonsymmorphic structures of CdTe and ZnTe are modelled and proposed to exhibit many interesting symmetry-enforced properties such as intrinsic persistent spin texture, band degeneracy, and reversible spin-polarization via ferroelectric switching ($\pm P$). These results have been explained using symmetry analysis supported by DFT calculations. To realize these unprecedented properties experimentally, (110) facets of bulk zinc-blende CdTe and ZnTe structures would be ideal to study as the symmetry of this particular growth direction of the crystal structure is invariant under non-symmorphic space group

operations. In the previous experiment, highly stable four atomic layers (4L) from (110) facets of the zinc-blende structure are exfoliated using a strategy involving a lamellar hybrid intermediate. [94] Experimental work confirmed that the ZnSe single layers possess a highly (110) preferred orientation and are highly stable at room temperature. Although there is structural distortion at the surface of the experimentally synthesized monolayers to minimize the surface energy, it will be interesting to study whether PSH can survive under such mechanical deformation. Since CdTe and ZnTe bulk structures are non-van der Waal solids and, hence, structural distortion of monolayer or a few layers at the surface is inevitable as experimentally found in the case of three atomic [95,96] and four atomic layers [94]. A four-atomic (4L) monolayer is cleaved from the (110) plane of zinc-blend CdTe and the atomic positions are relaxed. The side view of optimized structures is shown in Figure 10 which replicates the distorted structure reported in ref. [94]. The electronic properties are evaluated considering the spin-orbit coupling and the band structure is plotted in Figure 10. The band edges are located at the Brillouin zone centre and the spin splitting along $\Gamma \rightarrow Y$ direction remains unchanged. These results indicate (110) facets of zinc-blende structures of CdTe and ZnTe as presented in Figure S2 are ideal materials for realizing intrinsic PSH and thus realizing atomic thin non-ballistic spin field-effect-transistor. Further, these results indicate that symmetry-enforced properties are globally stable and can survive under large mechanical deformation. This is similar to symmetry-enforced band crossings in topological materials which exist due to nonsymmorphic symmetries alone, independent of the material details. [35–40]

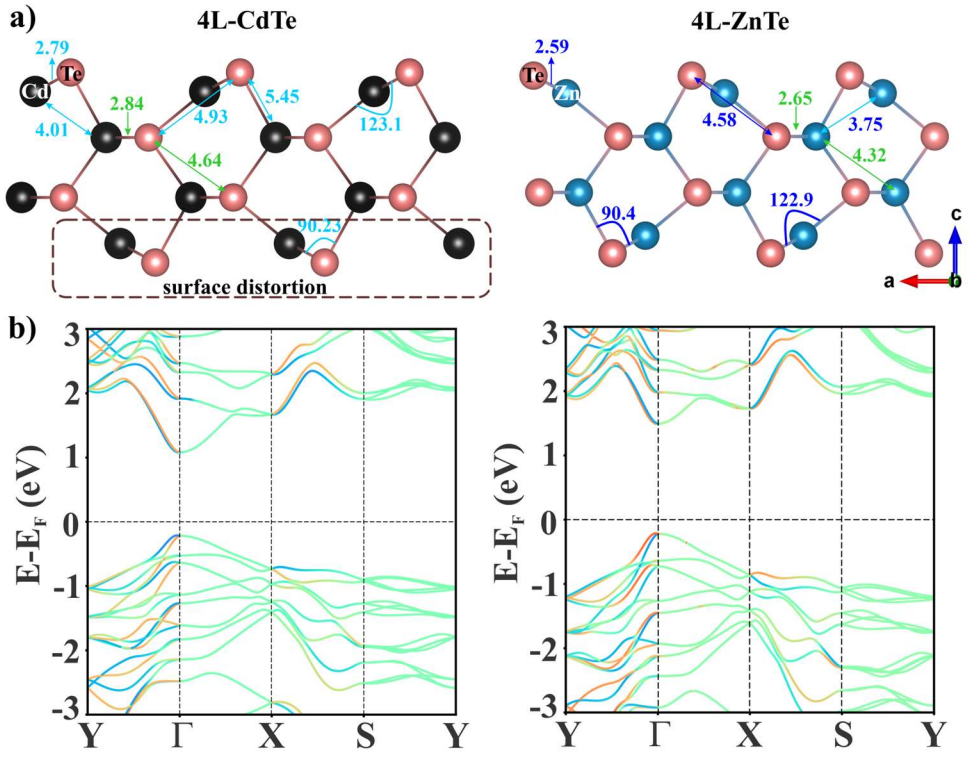

Figure 10 (a) Side view of four atomic thick (4L) CdTe and ZnTe structures replicating freestanding ZnSe synthesized from (110) facets of zinc-blende bulk crystal structure as in ref. [94] and (b) their electronic band structure incorporating a relativistic effect.

4. Conclusion:

In conclusion, two atomic thick nonsymmorphic crystal structures of CdTe and ZnTe are modelled in this work. These structures exhibit many interesting symmetry-enforced properties such as momentum-independent uniform spin polarization which leads to a long spin lifetime. The reversible spin-polarization via the ferroelectric switching. The pitch of PSH is calculated to be ~4-5 nm, and hence an ultrathin non-ballistic spin field-effect transistor can be designed. The PST in these structures was found to be robust against strain, layer thickness, and structural distortion. However, the PSH mode can be broken via a non-zero vertical electric field. A finite spin-Hall conductivity at the band edges and with such intriguing electronic properties can motivate experimentalists to design a ferromagnet-free spin-Hall effect transistor. Moreover, infinite spin lifetime in (110) facets of centuries-old tellurium-based zinc-blende semiconductors have been predicted in this work using group theory of solids supported by DFT and thus paves the way for the beginning of a new era in the field of spintronics.

5. Computational details

All calculations are performed using density functional theory (DFT) embedded in the VASP code. [97,98] The generalized gradient approximation (GGA) with Perdew-Burke-Ernzerhof (PBE) exchange-correlation interaction is used. [99] The projector-augmented plane waves (PAW) approach is employed to treat the ion-electron interaction. [100] The energy cut-off is set to 500 eV and the energy convergence is set to 10^{-8} eV. To obtain experimental geometries of 4L CdTe and ZnTe as in Figure 10, symmetry-constrained geometrical optimization is performed until the maximum force converges to 0.02 eV/Å. The Brillouin zone (BZ) is sampled with a 14×14×1 Γ-centered *k*-point mesh. A vacuum space of more than 20Å is added in the *z*-direction to eliminate periodic interaction between the layers. The second-order force constants are calculated using a 5×5×1 supercell sampled with 10×10×1 *k*-mesh using the finite difference method and plotted using the PHONOPY package. [101] PYPROCAR is used to plot spin texture. [102] The ferroelectric properties are calculated using the Berry phase method. [103–105] The spin Hall conductivity (SHC) is calculated from Berry curvature using a dense 200×200×1 *k*-mesh based on maximally localized Wannier function [106–111] by the formula [112]

$$\sigma_{xy}^{z} = \frac{e}{\hbar}\int_{Bz}\frac{dk}{(2\pi)^2}\Omega^{z}(k)$$

$\Omega^{z}(k)$ is the k-resolved term which is given by $\Omega^{z}(k) = \sum_n f_{kn}\Omega_n^z(k)$. Here, f_{kn} is the Fermi-Dirac distribution function for the *n*th band at k and $\Omega_n^z(k)$ is an analogue of the Berry curvature for the *n*th band given as;

$$\Omega_n^z(k) = \sum_{n'\neq n}\frac{2Im[\langle kn|j_x^z|kn'\rangle\langle kn'|v_y|kn\rangle]}{(\epsilon_{kn}-\epsilon_{kn'})^2}$$

Here, $j_x^z = \frac{1}{2}\{s_z, v\}$ is the spin current operator, $s_z = \frac{\hbar}{2}\sigma^z$ is the spin operator, v is the velocity operator and $|kn\rangle$ is the wave function of energy ϵ_{kn}.

Acknowledgement
MKM and PJ acknowledge financial support from the U.S. Department of Energy, Office of Basic Energy Sciences, Division of Materials Sciences and Engineering under Award No. DE-FG02-96ER45579. Resources of the National Energy Research Scientific Computing (NERSC) Center supported by the Office of Science of the U.S. Department of Energy under Contract No. DE-AC02-05CH11231 is also acknowledged. The authors extend their acknowledgment to the High-Performance Research Computing (HPRC) core facility at Virginia Commonwealth University for providing supercomputing resources.

References:

[1] X.-L. Qi and S.-C. Zhang, *Topological Insulators and Superconductors*, Rev Mod Phys **83**, 1057 (2011).
[2] F. Tang, H. C. Po, A. Vishwanath, and X. Wan, *Comprehensive Search for Topological Materials Using Symmetry Indicators*, Nature **566**, 486 (2019).
[3] K. S. Novoselov, A. K. Geim, S. V. Morozov, D. Jiang, Y. Zhang, S. V. Dubonos, I. V. Grigorieva, and A. A. Firsov, *Electric Field Effect in Atomically Thin Carbon Films*, Science **306**, 666 (2004).
[4] B. Radisavljevic, A. Radenovic, J. Brivio, V. Giacometti, and A. Kis, *Single-Layer MoS2 Transistors*, Nat. Nanotechnol. **6**, 147 (2011).
[5] S. Datta and B. Das, *Electronic Analog of the Electro-optic Modulator*, Appl. Phys. Lett. **56**, 665 (1990).
[6] W. Han, *Perspectives for Spintronics in 2D Materials*, APL Mater. **4**, 032401 (2016).
[7] I. Choudhuri, P. Bhauriyal, and B. Pathak, *Recent Advances in Graphene-like 2D Materials for Spintronics Applications*, Chem. Mater. **31**, 8260 (2019).
[8] Y. Liu, Y. Gao, S. Zhang, J. He, J. Yu, and Z. Liu, *Valleytronics in Transition Metal Dichalcogenides Materials*, Nano Res. **12**, 2695 (2019).
[9] J. R. Schaibley, H. Yu, G. Clark, P. Rivera, J. S. Ross, K. L. Seyler, W. Yao, and X. Xu, *Valleytronics in 2D Materials*, Nat. Rev. Mater. **1**, 16055 (2016).
[10] D. Xiao, G.-B. Liu, W. Feng, X. Xu, and W. Yao, *Coupled Spin and Valley Physics in Monolayers of MoS_2 and Other Group-vi Dichalcogenides*, Phys Rev Lett **108**, 196802 (2012).
[11] W. Yao, D. Xiao, and Q. Niu, *Valley-Dependent Optoelectronics from Inversion Symmetry Breaking*, Phys Rev B **77**, 235406 (2008).
[12] A. Manchon, H. C. Koo, J. Nitta, S. M. Frolov, and R. A. Duine, *New Perspectives for Rashba Spin–Orbit Coupling*, Nat. Mater. **14**, 871 (2015).
[13] J. D. Koralek, C. P. Weber, J. Orenstein, B. A. Bernevig, S.-C. Zhang, S. Mack, and D. D. Awschalom, *Emergence of the Persistent Spin Helix in Semiconductor Quantum Wells*, Nature **458**, 610 (2009).
[14] A. Sasaki, S. Nonaka, Y. Kunihashi, M. Kohda, T. Bauernfeind, T. Dollinger, K. Richter, and J. Nitta, *Direct Determination of Spin–Orbit Interaction Coefficients and Realization of the Persistent Spin Helix Symmetry*, Nat. Nanotechnol. **9**, 703 (2014).
[15] L. Zhu, Y. Zhang, P. Lin, Y. Wang, L. Yang, L. Chen, L. Wang, B. Chen, and Z. L. Wang, *Piezotronic Effect on Rashba Spin–Orbit Coupling in a ZnO/P3HT Nanowire Array Structure*, ACS Nano **12**, 1811 (2018).
[16] S. Datta, *How We Proposed the Spin Transistor*, Nat. Electron. **1**, 604 (2018).
[17] M. K. Mohanta, F. IS, A. Kishore, and A. De Sarkar, *Spin-Current Modulation in Hexagonal Buckled ZnTe and CdTe Monolayers for Self-Powered Flexible-Piezo-Spintronic Devices*, ACS Appl. Mater. Interfaces **13**, 40872 (2021).

[18] F. IS, M. K. Mohanta, and A. D. Sarkar, *Insights into Selected 2D Piezo Rashba Semiconductors for Self-Powered Flexible Piezo Spintronics: Material to Contact Properties*, J. Phys. Condens. Matter **35**, 253001 (2023).
[19] M. K. Mohanta, A. Arora, and A. De Sarkar, *Conflux of Tunable Rashba Effect and Piezoelectricity in Flexible Magnesium Monochalcogenide Monolayers for Next-Generation Spintronic Devices*, Nanoscale **13**, 8210 (2021).
[20] M. D'yakonov, *Spin Relaxation of Two-Dimensional Electrons in Non-Centrosymmetric Semiconductors*, Sov Phys Semicond **20**, 110 (1986).
[21] J. Schliemann, *Colloquium: Persistent Spin Textures in Semiconductor Nanostructures*, Rev Mod Phys **89**, 011001 (2017).
[22] J. Schliemann, J. C. Egues, and D. Loss, *Nonballistic Spin-Field-Effect Transistor*, Phys Rev Lett **90**, 146801 (2003).
[23] M. P. Walser, C. Reichl, W. Wegscheider, and G. Salis, *Direct Mapping of the Formation of a Persistent Spin Helix*, Nat. Phys. **8**, 757 (2012).
[24] M. Kohda, V. Lechner, Y. Kunihashi, T. Dollinger, P. Olbrich, C. Schönhuber, I. Caspers, V. V. Bel'kov, L. E. Golub, D. Weiss, K. Richter, J. Nitta and S. D. Ganichev, *Gate-Controlled Persistent Spin Helix State in (In,Ga)As Quantum Wells*, Phys Rev B **86**, 081306 (2012).
[25] F. Dettwiler, J. Fu, S. Mack, P. J. Weigele, J. C. Egues, D. D. Awschalom, and D. M. Zumbühl, *Stretchable Persistent Spin Helices in GaAs Quantum Wells*, Phys Rev X **7**, 031010 (2017).
[26] B. A. Bernevig, J. Orenstein, and S.-C. Zhang, *Exact SU(2) Symmetry and Persistent Spin Helix in a Spin-Orbit Coupled System*, Phys Rev Lett **97**, 236601 (2006).
[27] L. L. Tao and E. Y. Tsymbal, *Persistent Spin Texture Enforced by Symmetry*, Nat. Commun. **9**, 2763 (2018).
[28] C. Autieri, P. Barone, J. Slawińska, and S. Picozzi, *Persistent Spin Helix in Rashba-Dresselhaus Ferroelectric CsBiNb2O7*, Phys Rev Mater **3**, 084416 (2019).
[29] H. Ai, X. Ma, X. Shao, W. Li, and M. Zhao, *Reversible Out-of-Plane Spin Texture in a Two-Dimensional Ferroelectric Material for Persistent Spin Helix*, Phys Rev Mater **3**, 054407 (2019).
[30] Moh. A. U. Absor and F. Ishii, *Doping-Induced Persistent Spin Helix with a Large Spin Splitting in Monolayer SnSe*, Phys Rev B **99**, 075136 (2019).
[31] Moh. A. U. Absor and F. Ishii, *Intrinsic Persistent Spin Helix State in Two-Dimensional Group-IV Monochalcogenide MX Monolayers (M=Sn or Ge and X=S, Se, or Te)*, Phys Rev B **100**, 115104 (2019).
[32] H. Lee, J. Im, and H. Jin, *Emergence of the Giant Out-of-Plane Rashba Effect and Tunable Nanoscale Persistent Spin Helix in Ferroelectric SnTe Thin Films*, Appl. Phys. Lett. **116**, 022411 (2020).
[33] C. Bradley and A. Cracknell, *The Mathematical Theory of Symmetry in Solids: Representation Theory for Point Groups and Space Groups* (Oxford University Press, 2010).
[34] See Supplemental Material at xxxxxxx for schematic of two non-symmorphic space group symmetries; (a) glide plane and (b) screw axis, geometrical view of (110) plane in zinc-blende bulk CdTe structure, general positions of space group no. 31, detailed analysis of symmetry operations in non-symmorphic space group no. 31, SU(2) group, some properties of time reversal operator.
[35] Y. X. Zhao and A. P. Schnyder, *Nonsymmorphic Symmetry-Required Band Crossings in Topological Semimetals*, Phys Rev B **94**, 195109 (2016).
[36] L. Michel and J. Zak, *Connectivity of Energy Bands in Crystals*, Phys Rev B **59**, 5998 (1999).
[37] S. M. Young and C. L. Kane, *Dirac Semimetals in Two Dimensions*, Phys Rev Lett **115**, 126803 (2015).
[38] A. Furusaki, *Weyl Points and Dirac Lines Protected by Multiple Screw Rotations*, Sci. Bull. **62**, 788 (2017).
[39] B.-J. Yang, T. A. Bojesen, T. Morimoto, and A. Furusaki, *Topological Semimetals Protected by Off-Centered Symmetries in Nonsymmorphic Crystals*, Phys Rev B **95**, 075135 (2017).

[40] H. Wu, A. M. Hallas, X. Cai, J. Huang, J. S. Oh, V. Loganathan, A. Weiland, G. T. McCandless, J. Y. Chan, S.-K. Mo, D. Lu, M. Hashimoto, J. Denlinger, R. J. Birgeneau, A. H. Nevidomskyy, G. Li, E. Morosan and M. Yi, *Nonsymmorphic Symmetry-Protected Band Crossings in a Square-Net Metal PtPb4*, Npj Quantum Mater. **7**, 31 (2022).
[41] G. Dresselhaus, *Spin-Orbit Coupling Effects in Zinc Blende Structures*, Phys Rev **100**, 580 (1955).
[42] B. Jusserand, D. Richards, G. Allan, C. Priester, and B. Etienne, *Spin Orientation at Semiconductor Heterointerfaces*, Phys Rev B **51**, 4707 (1995).
[43] S. D. Ganichev, V. V. Bel'kov, L. E. Golub, E. L. Ivchenko, P. Schneider, S. Giglberger, J. Eroms, J. De Boeck, G. Borghs, W. Wegscheider, D. Weiss and W. Prettl, *Experimental Separation of Rashba and Dresselhaus Spin Splittings in Semiconductor Quantum Wells*, Phys Rev Lett **92**, 256601 (2004).
[44] J. B. Miller, D. M. Zumbühl, C. M. Marcus, Y. B. Lyanda-Geller, D. Goldhaber-Gordon, K. Campman, and A. C. Gossard, *Gate-Controlled Spin-Orbit Quantum Interference Effects in Lateral Transport*, Phys Rev Lett **90**, 076807 (2003).
[45] Y. A. Bychkov and É. I. Rashba, *Properties of a 2D Electron Gas with Lifted Spectral Degeneracy*, JETP Lett **39**, 78 (1984).
[46] J. Schliemann and D. Loss, *Anisotropic Transport in a Two-Dimensional Electron Gas in the Presence of Spin-Orbit Coupling*, Phys Rev B **68**, 165311 (2003).
[47] M. Trushin and J. Schliemann, *Spin Dynamics in Rolled-up Two-Dimensional Electron Gases*, New J. Phys. **9**, 346 (2007).
[48] K.-H. Jin, E. Oh, R. Stania, F. Liu, and H. W. Yeom, *Enhanced Berry Curvature Dipole and Persistent Spin Texture in the Bi(110) Monolayer*, Nano Lett. **21**, 9468 (2021).
[49] J. Sławińska, F. T. Cerasoli, P. Gopal, M. Costa, S. Curtarolo, and M. B. Nardelli, *Ultrathin SnTe Films as a Route towards All-in-One Spintronics Devices*, 2D Mater. **7**, 025026 (2020).
[50] A. Jain, S. P. Ong, G. Hautier, W. Chen, W. D. Richards, S. Dacek, S. Cholia, D. Gunter, D. Skinner, G. Ceder and K. A. Persson, *Commentary: The Materials Project: A Materials Genome Approach to Accelerating Materials Innovation*, APL Mater. **1**, 011002 (2013).
[51] Z. S. Popović, J. M. Kurdestany, and S. Satpathy, *Electronic Structure and Anisotropic Rashba Spin-Orbit Coupling in Monolayer Black Phosphorus*, Phys Rev B **92**, 035135 (2015).
[52] L. C. Gomes and A. Carvalho, *Phosphorene Analogues: Isoelectronic Two-Dimensional Group-IV Monochalcogenides with Orthorhombic Structure*, Phys Rev B **92**, 085406 (2015).
[53] J. Kim, K.-W. Kim, D. Shin, S.-H. Lee, J. Sinova, N. Park, and H. Jin, *Prediction of Ferroelectricity-Driven Berry Curvature Enabling Charge- and Spin-Controllable Photocurrent in Tin Telluride Monolayers*, Nat. Commun. **10**, 3965 (2019).
[54] C. Rinaldi, S. Varotto, M. Asa, J. Sławińska, J. Fujii, G. Vinai, S. Cecchi, D. Di Sante, R. Calarco, I. Vobornik, G. Panaccione, S. Picozzi and R. Bertacco, *Ferroelectric Control of the Spin Texture in GeTe*, Nano Lett. **18**, 2751 (2018).
[55] G. Bian, X. Wang, T. Miller, T.-C. Chiang, P. J. Kowalczyk, O. Mahapatra, and S. A. Brown, *First-Principles and Spectroscopic Studies of Bi(110) Films: Thickness-Dependent Dirac Modes and Property Oscillations*, Phys Rev B **90**, 195409 (2014).
[56] K.-H. Jin, H. Huang, Z. Wang, and F. Liu, *A 2D Nonsymmorphic Dirac Semimetal in a Chemically Modified Group-VA Monolayer with a Black Phosphorene Structure*, Nanoscale **11**, 7256 (2019).
[57] M. Kim, J. Im, A. J. Freeman, J. Ihm, and H. Jin, *Switchable S = 1/2 and J = 1/2 Rashba Bands in Ferroelectric Halide Perovskites*, Proc. Natl. Acad. Sci. **111**, 6900 (2014).
[58] L. Zhang, C. Tang, C. Zhang, and A. Du, *First-Principles Screening of Novel Ferroelectric MXene Phases with a Large Piezoelectric Response and Unusual Auxeticity*, Nanoscale **12**, 21291 (2020).
[59] W. Ding, J. Zhu, Z. Wang, Y. Gao, D. Xiao, Y. Gu, Z. Zhang, and W. Zhu, *Prediction of Intrinsic Two-Dimensional Ferroelectrics in In 2 Se 3 and Other III 2 -VI 3 van Der Waals Materials*, Nat. Commun. **8**, 1 (2017).

[60] R. Fei, W. Kang, and L. Yang, *Ferroelectricity and Phase Transitions in Monolayer Group-IV Monochalcogenides*, Phys Rev Lett **117**, 097601 (2016).
[61] A. Splendiani, L. Sun, Y. Zhang, T. Li, J. Kim, C.-Y. Chim, G. Galli, and F. Wang, *Emerging Photoluminescence in Monolayer MoS2*, Nano Lett. **10**, 1271 (2010).
[62] J. Park, M. S. Kim, E. Cha, J. Kim, and W. Choi, *Synthesis of Uniform Single Layer WS2 for Tunable Photoluminescence*, Sci. Rep. **7**, 16121 (2017).
[63] J. Britt and C. Ferekides, *Thin-film CdS/CdTe Solar Cell with 15.8% Efficiency*, Appl. Phys. Lett. **62**, 2851 (1993).
[64] T. Aramoto, S. Kumazawa, H. Higuchi, T. Arita, S. Shibutani, T. Nishio, J. Nakajima, M. Tsuji, A. Hanafusa, T. Hibino, K. Omura, H. Ohyama and M. Murozono, *16.0% Efficient Thin-Film CdS/CdTe Solar Cells*, Jpn. J. Appl. Phys. **36**, 6304 (1997).
[65] A. Bosio, G. Rosa, and N. Romeo, *Past, Present and Future of the Thin Film CdTe/CdS Solar Cells*, Sol. Energy **175**, 31 (2018).
[66] R. G. Chaudhuri, A. Chaturvedi, and E. Iype, *Visible Light Active 2D C3N4-CdS Hetero-Junction Photocatalyst for Effective Removal of Azo Dye by Photodegradation*, Mater. Res. Express **5**, 036202 (2018).
[67] Q.-Q. Bi, J.-W. Wang, J.-X. Lv, J. Wang, W. Zhang, and T.-B. Lu, *Selective Photocatalytic CO2 Reduction in Water by Electrostatic Assembly of CdS Nanocrystals with a Dinuclear Cobalt Catalyst*, ACS Catal. **8**, 11815 (2018).
[68] P. Garg, S. Kumar, I. Choudhuri, A. Mahata, and B. Pathak, *Hexagonal Planar CdS Monolayer Sheet for Visible Light Photocatalysis*, J. Phys. Chem. C **120**, 7052 (2016).
[69] I. Repins, M. A. Contreras, B. Egaas, C. DeHart, J. Scharf, C. L. Perkins, B. To, and R. Noufi, *19·9%-Efficient ZnO/CdS/CuInGaSe2 Solar Cell with 81·2% Fill Factor*, Prog. Photovolt. Res. Appl. **16**, 235 (2008).
[70] K. Wu, J. Chen, H. Ma, L. Wan, W. Hu, and J. Yang, *Two-Dimensional Giant Tunable Rashba Semiconductors with Two-Atom-Thick Buckled Honeycomb Structure*, Nano Lett. **21**, 740 (2021).
[71] M. A. U. Absor, A. Lukmantoro, and I. Santoso, *Full-Zone Persistent Spin Textures with Giant Spin Splitting in Two-Dimensional Group IV–V Compounds*, J. Phys. Condens. Matter **34**, 445501 (2022).
[72] S. Singh and A. H. Romero, *Giant Tunable Rashba Spin Splitting in a Two-Dimensional BiSb Monolayer and in BiSb/AlN Heterostructures*, Phys Rev B **95**, 165444 (2017).
[73] S. Sheoran, S. Monga, A. Phutela, and S. Bhattacharya, *Coupled Spin-Valley, Rashba Effect, and Hidden Spin Polarization in WSi2N4 Family*, J. Phys. Chem. Lett. **14**, 1494 (2023).
[74] Q.-F. Yao, J. Cai, W.-Y. Tong, S.-J. Gong, J.-Q. Wang, X. Wan, C.-G. Duan, and J. H. Chu, *Manipulation of the Large Rashba Spin Splitting in Polar Two-Dimensional Transition-Metal Dichalcogenides*, Phys Rev B **95**, 165401 (2017).
[75] L. Xiang, Y. Ke, and Q. Zhang, *Tunable Giant Rashba-Type Spin Splitting in PtSe2/MoSe2 Heterostructure*, Appl. Phys. Lett. **115**, 203501 (2019).
[76] Y. Ma, Y. Dai, W. Wei, X. Li, and B. Huang, *Emergence of Electric Polarity in BiTeX (X = Br and I) Monolayers and the Giant Rashba Spin Splitting*, Phys Chem Chem Phys **16**, 17603 (2014).
[77] N. Higashitarumizu, H. Kawamoto, C.-J. Lee, B.-H. Lin, F.-H. Chu, I. Yonemori, T. Nishimura, K. Wakabayashi, W.-H. Chang, and K. Nagashio, *Purely In-Plane Ferroelectricity in Monolayer SnS at Room Temperature*, Nat. Commun. **11**, 2428 (2020).
[78] X. Cartoixà, D. Z.-Y. Ting, and Y.-C. Chang, *A Resonant Spin Lifetime Transistor*, Appl. Phys. Lett. **83**, 1462 (2003).
[79] M. Khazaei, A. Ranjbar, M. Ghorbani-Asl, M. Arai, T. Sasaki, Y. Liang, and S. Yunoki, *Nearly Free Electron States in MXenes*, Phys Rev B **93**, 205125 (2016).
[80] M. K. Mohanta, I. S. Fathima, and A. De Sarkar, *Exceptional Mechano-Electronic Properties in the HfN2 Monolayer: A Promising Candidate in Low-Power Flexible Electronics, Memory Devices and Photocatalysis*, Phys Chem Chem Phys **22**, 21275 (2020).

[81] M. A. U. Absor, Y. Faishal, M. Anshory, I. Santoso, Sholihun, Harsojo, and F. Ishii, *Highly Persistent Spin Textures with Giant Tunable Spin Splitting in the Two-Dimensional Germanium Monochalcogenides*, J. Phys. Condens. Matter **33**, 305501 (2021).
[82] J. E. Hirsch, *Spin Hall Effect*, Phys Rev Lett **83**, 1834 (1999).
[83] J. Wunderlich, B.-G. Park, A. C. Irvine, L. P. Zârbo, E. Rozkotová, P. Nemec, V. Novák, J. Sinova, and T. Jungwirth, *Spin Hall Effect Transistor*, Science **330**, 1801 (2010).
[84] J. Wunderlich, A. C. Irvine, J. Sinova, B. G. Park, L. P. Zârbo, X. L. Xu, B. Kaestner, V. Novák, and T. Jungwirth, *Spin-Injection Hall Effect in a Planar Photovoltaic Cell*, Nat. Phys. **5**, 675 (2009).
[85] O. Çakıroğlu, J. O. Island, Y. Xie, R. Frisenda, and A. Castellanos-Gomez, *An Automated System for Strain Engineering and Straintronics of 2D Materials*, Adv. Mater. Technol. **8**, 2201091 (2023).
[86] Y. Han, J. Zhou, H. Wang, L. Gao, S. Feng, K. Cao, Z. Xu, and Y. Lu, *Experimental Nanomechanics of 2D Materials for Strain Engineering*, Appl. Nanosci. **11**, 1075 (2021).
[87] Z. Peng, X. Chen, Y. Fan, D. J. Srolovitz, and D. Lei, *Strain Engineering of 2D Semiconductors and Graphene: From Strain Fields to Band-Structure Tuning and Photonic Applications*, Light Sci. Appl. **9**, 190 (2020).
[88] Y. Wang, C. Cong, W. Yang, J. Shang, N. Peimyoo, Y. Chen, J. Kang, J. Wang, W. Huang, and T. Yu, *Strain-Induced Direct–Indirect Bandgap Transition and Phonon Modulation in Monolayer WS2*, Nano Res. **8**, 2562 (2015).
[89] M. Dienwiebel, G. S. Verhoeven, N. Pradeep, J. W. M. Frenken, J. A. Heimberg, and H. W. Zandbergen, *Superlubricity of Graphite*, Phys. Rev. Lett. **92**, 126101 (2004).
[90] M. Yankowitz, K. Watanabe, T. Taniguchi, P. San-Jose, and B. J. LeRoy, *Pressure-Induced Commensurate Stacking of Graphene on Boron Nitride*, Nat. Commun. **7**, 13168 (2016).
[91] S. M. Clark, K.-J. Jeon, J.-Y. Chen, and C.-S. Yoo, *Few-Layer Graphene under High Pressure: Raman and X-Ray Diffraction Studies*, Solid State Commun. **154**, 15 (2013).
[92] S. Yang, Y. Chen, and C. Jiang, *Strain Engineering of Two-Dimensional Materials: Methods, Properties, and Applications*, InfoMat **3**, 397 (2021).
[93] M. K. Mohanta and A. De Sarkar, *Coupled Spin and Valley Polarization in Monolayer HfN2 and Valley-Contrasting Physics at the HfN2-WSe2 Interface*, Phys Rev B **102**, 125414 (2020).
[94] Y. Sun, Z. Sun, S. Gao, H. Cheng, Q. Liu, J. Piao, T. Yao, C. Wu, S. Hu, S. Wei and Y. Xie, *Fabrication of Flexible and Freestanding Zinc Chalcogenide Single Layers*, Nat. Commun. **3**, 1057 (2012).
[95] E. A. Soares, V. E. de Carvalho, and V. B. Nascimento, *A Layer-by-Layer Study of CdTe(110) Surface Debye Temperature and Thermal Vibrations by Low Energy Electron Diffraction*, Surf. Sci. **431**, 74 (1999).
[96] K. Watari, J. L. A. Alves, and A. C. Ferraz, *Atomic Structures of CdTe and CdSe (110) Surfaces*, Braz. J. Phys. **26**, 271 (1996).
[97] G. Kresse and J. Furthmüller, *Efficient Iterative Schemes for Ab Initio Total-Energy Calculations Using a Plane-Wave Basis Set*, Phys. Rev. B **54**, 11169 (1996).
[98] G. Kresse and J. Furthmüller, *Efficiency of Ab-Initio Total Energy Calculations for Metals and Semiconductors Using a Plane-Wave Basis Set*, Comput. Mater. Sci. **6**, 15 (1996).
[99] J. P. Perdew, K. Burke, and M. Ernzerhof, *Generalized Gradient Approximation Made Simple*, Phys. Rev. Lett. **77**, 3865 (1996).
[100] P. E. Blöchl, *Projector Augmented-Wave Method*, Phys. Rev. B **50**, 17953 (1994).
[101] A. Togo and I. Tanaka, *First Principles Phonon Calculations in Materials Science*, Scr. Mater. **108**, 1 (2015).
[102] U. Herath, P. Tavadze, X. He, E. Bousquet, S. Singh, F. Muñoz, and A. H. Romero, *PyProcar: A Python Library for Electronic Structure Pre/Post-Processing*, Comput. Phys. Commun. **251**, 107080 (2020).
[103] R. Resta, *Theory of the Electric Polarization in Crystals*, Ferroelectrics **136**, 51 (1992).
[104] R. Resta, *Macroscopic Polarization in Crystalline Dielectrics: The Geometric Phase Approach*, Rev Mod Phys **66**, 899 (1994).

[105] R. D. King-Smith and D. Vanderbilt, *Theory of Polarization of Crystalline Solids*, Phys Rev B **47**, 1651 (1993).
[106] J. Qiao, J. Zhou, Z. Yuan, and W. Zhao, *Calculation of Intrinsic Spin Hall Conductivity by Wannier Interpolation*, Phys Rev B **98**, 214402 (2018).
[107] A. A. Mostofi, J. R. Yates, Y.-S. Lee, I. Souza, D. Vanderbilt, and N. Marzari, *Wannier90: A Tool for Obtaining Maximally-Localised Wannier Functions*, Comput. Phys. Commun. **178**, 685 (2008).
[108] G. Pizzi, V. Vitale, R. Arita, S. Blügel, F. Freimuth, G. Géranton, M. Gibertini, D. Gresch, C. Johnson, T. Koretsune, J. Ibañez-Azpiroz, H. Lee, J.-M. Lihm, D. Marchand, A. Marrazzo, Y. Mokrousov, J. I. Mustafa, Y. Nohara, Y. Nomura, L. Paulatto, S. Poncé, T. Ponweiser, J. Qiao, F. Thöle, S. S. Tsirkin, M. Wierzbowska, N. Marzari, D. Vanderbilt, I. Souza, A. A. Mostofi and J. R. Yates, *Wannier90 as a Community Code: New Features and Applications*, J. Phys. Condens. Matter **32**, 165902 (2020).
[109] A. Damle, L. Lin, and L. Ying, *SCDM-k: Localized Orbitals for Solids via Selected Columns of the Density Matrix*, J. Comput. Phys. **334**, 1 (2017).
[110] P. Giannozzi, O. Andreussi, T. Brumme, O. Bunau, M. B. Nardelli, M. Calandra, R. Car, C. Cavazzoni, D. Ceresoli, M. Cococcioni, N. Colonna, I. Carnimeo, A. D. Corso, S. de Gironcoli, P. Delugas, R. A. DiStasio, A. Ferretti, A. Floris, G. Fratesi, G. Fugallo, R. Gebauer, U. Gerstmann, F. Giustino, T. Gorni, J. Jia, M. Kawamura, H.-Y. Ko, A. Kokalj, E. Küçükbenli, M. Lazzeri, M. Marsili, N. Marzari, F. Mauri, N. L. Nguyen, H.-V. Nguyen, A. Otero-de-la-Roza, L. Paulatto, S. Poncé, D. Rocca, R. Sabatini, B. Santra, M. Schlipf, A. P. Seitsonen, A. Smogunov, I. Timrov, T. Thonhauser, P. Umari, N. Vast, X. Wu and S. Baroni, *Advanced Capabilities for Materials Modelling with Quantum ESPRESSO*, J. Phys. Condens. Matter **29**, 465901 (2017).
[111] P. Giannozzi, S. Baroni, N. Bonini, M. Calandra, R. Car, C. Cavazzoni, D. Ceresoli, G. L. Chiarotti, M. Cococcioni, I. Dabo, A. D. Corso, S. de Gironcoli, S. Fabris, G. Fratesi, R. Gebauer, U. Gerstmann, C. Gougoussis, A. Kokalj, M. Lazzeri, L. Martin-Samos, N. Marzari, F. Mauri, R. Mazzarello, S. Paolini, A. Pasquarello, L. Paulatto, C. Sbraccia, S. Scandolo, G. Sclauzero, A. P. Seitsonen, A. Smogunov, P. Umari and R. M. Wentzcovitch, *QUANTUM ESPRESSO: A Modular and Open-Source Software Project for Quantum Simulations of Materials*, J. Phys. Condens. Matter **21**, 395502 (2009).
[112] G. Y. Guo, S. Murakami, T.-W. Chen, and N. Nagaosa, *Intrinsic Spin Hall Effect in Platinum: First-Principles Calculations*, Phys Rev Lett **100**, 096401 (2008).